LASER & PHOTONICS REVIEWS
www.lpr-journal.org

A Sixteen-user Time-bin Entangled Quantum Communication Network With Fully Connected Topology

Yiwen Huang, Zhantong Qi, Yilin Yang, Yuting Zhang, Yuanhua Li, Yuanlin Zheng, and Xianfeng Chen**

Quantum key distribution (QKD) promises unconditionally information-theoretic secure communication guaranteed by the laws of physics and has become one of the most crucial candidates in future security aspects. Developing a large-scale network with a scalable and integrated scheme is of great significance for expanding the advantages of QKD protocols among multiple users. Here, a sixteen-user fully connected quantum network by using a novel time-bin entangled source implemented in the integrated multi-channel periodically poled lithium niobate waveguides is proposed. Based on this entangled source, the quantum processor prepares 120 entangled photon pairs to allocate 15 links to each user by utilizing dense wavelength division multiplexing technology. To enable the users' communication with each other simultaneously, a phase-compensated Mach-Zehnder Interferometer based on a Fourier-transform setup to control the relative phase of the interferometer for all the involved wavelength channels is developed. The experimental results show that the network can support sixteen users for long-distance communication with each other simultaneously. The novel scheme of time-bin entangled sources paves an efficient way for implementing large-scale quantum resources in a compact integrated platform, and the time-bin entangled network promises a new potential for constructing large-scale and extensible quantum networks with an integrated photonic architecture.

1. Introduction

Quantum key distribution (QKD) technology is an inevitable choice for future secure communication due to its information-theoretic security with the nature of quantum physics.[1–3] Thus far, as the QKD technology has gradually reached a mature level,[4–8] how to realize a large-scale quantum communication network effectively has become a thriving research field.[9,10] To date, there are already several categories of quantum network configurations, such as quantum repeater networks based on trusted nodes, point-to-point networks,[11,12] point-to-multipoint networks,[13,14] and fully connected networks.[15] As the paradigmatic quantum mechanical resource, quantum entanglement has become the key ingredient in many quantum-information tasks, such as quantum repeaters,[16] teleportation,[17–19] QKD,[20] and entanglement swapping.[21] Entanglement-based quantum network offers the promise platform for many dramatic applications,[22,23] such as distributed quantum computation,[24] quantum sensing,[25] and multi-user communication. Experimental advances in entanglement-based quantum technique open up the possibility of a fully connected quantum Internet, which may revolutionize the way of information exchange in the future.

The future quantum network will be a multi-user, scalable, secure and widespread connectivity network, and should integrate different transmission links, such as satellite communication, ground-based free space communication, and long-distance optical fiber communication links.[26,27] Recently, the fully connected quantum communication network based on quantum entanglement has attracted much attention in constructing a large-scale metropolitan network. Such type of network configuration enables users' communication with each other at the same time when minimizing the infrastructure and

Y. Huang, Z. Qi, Y. Yang, Y. Zhang, Y. Li, Y. Zheng, X. Chen
State Key Laboratory of Advanced Optical Communication Systems and Networks
School of Physics and Astronomy
Shanghai Jiao Tong University
Shanghai 200240, China
E-mail: lyhua1984@shiep.edu.cn; xfchen@sjtu.edu.cn

The ORCID identification number(s) for the author(s) of this article can be found under https://doi.org/10.1002/lpor.202301026

DOI: 10.1002/lpor.202301026

Y. Li
Department of Physics
Shanghai Key Laboratory of Materials Protection and Advanced Materials in Electric Power
Shanghai University of Electric Power
Shanghai 200090, China

Y. Zheng, X. Chen
Shanghai Research Center for Quantum Sciences
Shanghai 201315, China

X. Chen
Collaborative Innovation Center of Light Manipulation and Applications
Shandong Normal University
Jinan 250358, China

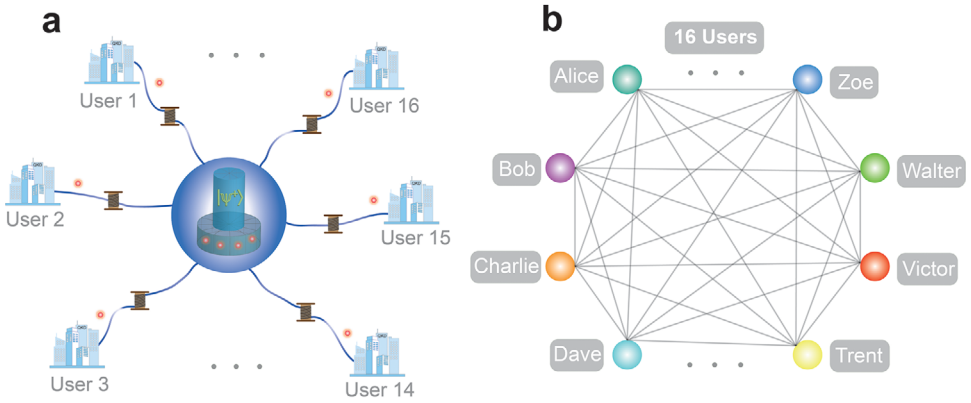

Figure 1. Conceptual illustration of the fully connected network architecture. a) Structure of the physical topology of the network. b) Structure of the communication topology of the network.

hardware.[28,29] Polarization-entangled fully connected QKD network was demonstrated experimentally by using a Sagnac-type polarization-entangled source and dense wavelength division multiplexing (DWDM) technology.[15,28] However, in this category of entanglement-based fully connected networks, the number of quantum correlations and communication links becomes increasingly complex and grows quadratically in demand as the number of users increases. Although the scheme of using passive beam splitters to probabilistically distribute entangled photon pairs between the users can significantly relax the requirement of quantum resources,[30] the intrinsic loss from the beam splitters would reduce the signal-to-noise ratio and secure the key rate of the corresponding two-party communication. How to flexibly provide enough quantum resources becomes an urgent and important issue for constructing the large-scale quantum communication network.

Here we propose a sixteen-user quantum network with a fully connected architecture by using DWDM technology and a time-bin entangled source based on integrated periodically poled lithium niobate (PPLN) waveguides. To effectively implement the fully connected network topology, we develop a novel time-bin entangled source based on integrated multi-channel PPLN waveguides and prepare 120 entangled photon pairs to allocate 15 links to each user by utilizing dense wavelength division multiplexing technology. Besides, we designed a phase-compensated Mach-Zehnder Interferometer (MZI) based on a Fourier-transform setup to enable the end users to communicate with each other simultaneously. The novel scheme of time-bin entangled sources implemented in integrated multi-channel PPLN waveguides can easily obtain large amounts of quantum resources while maintaining the simple structure and compact size of the quantum system. Our time-bin entangled network paves a novel way for constructing large-scale and extensible quantum networks with an integrated photonic architecture, which provides a new option to construct QKD interconnected networks with dense users in metropolitan areas.

2. Network Architecture and Experimental Setup

The time-bin entanglement-based network architecture can be conceptually understood as the superposition of physical layer and communication layer, as presented in **Figure 1**. The physical layer consists of all the hardware shown in **Figure 2**, mainly including the waveguide-based time-bin entanglement source, the multiplexing and demultiplexing module for photon pairs allocation, single transmission fibers for entanglement distribution, and the entanglement detection modules. At its very core, the quantum processor is responsible for the fabrication of entangled photon pairs and distribution to the remote end users. Each user is equipped with an MZI and 2 single-photon detectors, exactly the same as in standard two-party quantum communication schemes. In the communication layer, each pair of users can leverage the multiplexed photon pairs to generate secure keys with the assistance of classical communication technologies.

To implement the fully connected network architecture with N users, a minimum of $N(N-1)/2$ quantum correlated photon pairs are required. The quantum processor multiplexes $N-1$ channels into each single-mode fiber for each user so that all the users can share a time-bin entangled state with every other user. For a sixteen-user fully connected network, 120 quantum correlated links at the C-band are needed, which is quite difficult for an entangled source by pumping a nonlinear crystal. As the number of users increases, the physical topology of the resulting network remains elementary and grows linearly because all channels needed by each user are multiplexed into the same single-mode fiber, while the structure of the communication layer and number of required quantum links becomes increasingly complex and grows quadratically. Preparing enough quantum-correlated links at C-band with the minimal system loss becomes an important technique. An effective approach to implement this functionality is to adopt photonic integrated circuits, e.g., high-efficiency waveguide structures.[31,32] We developed a time-bin entangled source at telecommunications wavelengths based on integrated PPLN waveguides to construct a fully connected network.

The experimental setup is depicted in Figure 2. A picosecond pulse laser at 1545.3 nm with a repetition frequency of 80 MHz is launched into a 1-GHZ unbalanced Mach-Zehnder interferometer (MZI), to create double pulses with the time modes of t_0 for the short arm and t_1 for the long arm, respectively. Then, the double pulses are frequency doubled in a type-0 PPLN waveguide by second-harmonic generation. The second harmonic is split into 6 components and coupled to the 6 nominally identical integrated PPLN waveguides to generate entangled photon pairs

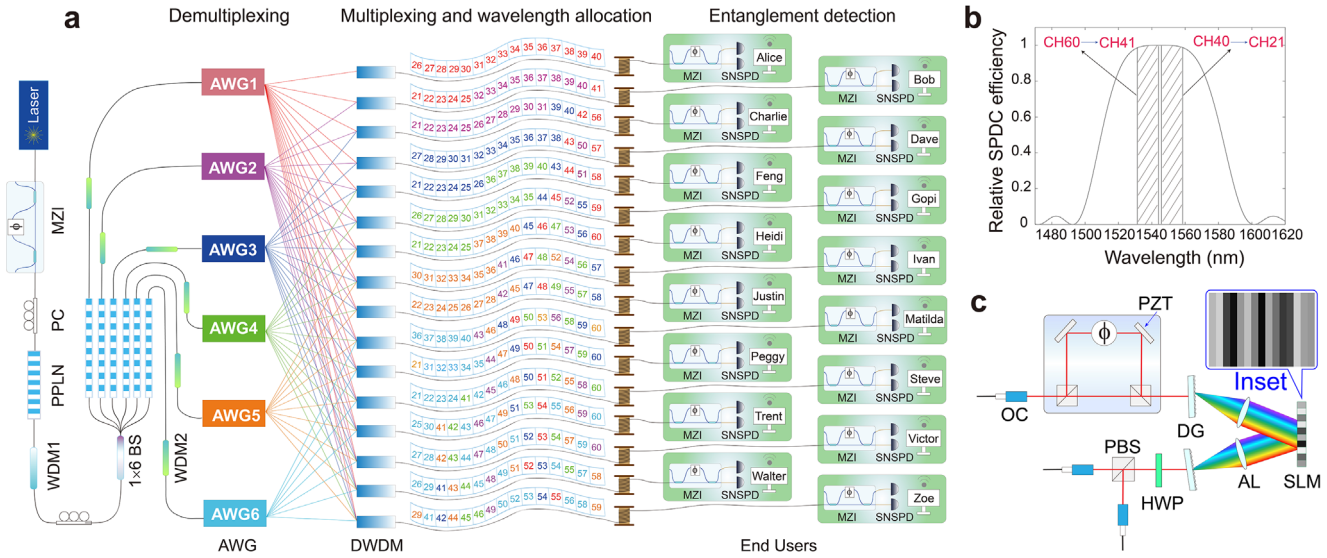

Figure 2. Experimental setup for the sixteen-user fully connected QKD network. a) Experimental setup. The specific ITU wavelength channels of all users are presented in the wavelength allocation part, in which the color numbers indicate the 100-GHz DWDM channels multiplexed from the representative-colored AWGs. One can easily distinguish the entangled photon pairs according to the ITU channel numbers, which add up to 81 for every photon pair like {CH40, CH41} and {CH21, CH60}. b) Typical spectrum of the SPDC source based on PPLN waveguide. The curve is the theoretical result calculated by using the Sellmeier equation.[33] c) Schematic of the MZIs for the end users. Inset: The diagram loaded on Alice's SLM to control the relative phases to be zero for the fifteen wavelength channels. MZI, 1-GHz unbalanced Mach-Zehnder interferometer; PC, polarization controller; WDM, wavelength division multiplexing filter; AWG, arrayed waveguide grating; BS, beam splitter; DWDM, dense wavelength division multiplexing filter; SNSPD, superconducting single photon detector. OC: Optical collimator; BS: 50:50 beam splitter; PZT: Piezoelectric transducer; PBS: polarization beam splitter; DG: Diffraction grating; SLM: Spatial light modulator; AL: Achromatic lens; HWP, half-wave plate.

by spontaneous parametric down-conversion (SPDC) process. One can express the superposition state of the photon pairs emitted at different temporal modes denoted by t_0 and t_1 as $|\phi\rangle = 1/\sqrt{2}\ (|t\rangle_0|t\rangle_0 + e^{2i\theta}|t\rangle_1|t\rangle_1)$, where θ is the phase of the MZI. The main parameters of the on-chip PPLN waveguides are listed in **Table 1**, in which the efficiency of the nonlinear processes is measured by using a continuous wave at 1545.3 nm. Because of the weak dispersion at the telecommunication wavelength of PPLN waveguides, the spectrum spans a full width at a maximum of ≈70 nm, covering the whole telecom C- and L-band. The spectrum of the SPDC photons is symmetric with respect to the central wavelength of 1545.3 nm, which corresponds to the central wavelength between the International Telecommunication Union (ITU) 100 GHz DWDM grid of channel 40 and channel 41. Due to energy conservation during the SPDC processes, the photon pairs are naturally frequency-time entangled with the state of frequency anticorrelated biphoton states. Thus, we can obtain time-bin entangled photon pairs of {CH40, CH41}, {CH39, CH42}, and so on.

Table 1. Main parameters of the PPLN waveguides.

Waveguides	SHG efficiency [%/W]	SPDC spectral brightness [pairs/nm/mW]
PPLN 1	450	1.7×10^8
PPLN 2	300	7.2×10^7
PPLN 3	500	1.9×10^8
PPLN 4	250	6.5×10^7
PPLN 5	400	1.1×10^8
PPLN 6	350	8.7×10^7

To implement the network architecture with a fully connected topological graph in Figure 1b, we first use 6 identical arrayed waveguide gratings (AWG) that cover the ITU channels of CH21-CH60 to divert the signal and idler photons generated in each PPLN waveguide into 20 entangled photon pairs, i.e., CH21 to CH40 for idler and CH41 to CH60 for signal. Then, sixteen thin-film DWDM filters with fifteen different wavelength channels are leveraged to multiplex 15 designed wavelength channels together in the single mode fibers to distribute to the end users. It is essential to ensure the fifteen photon channels of each user received from the quantum processor are entangled with other users, respectively. To achieve this, we first allocate fifteen signal channels from the SPDC source to user Alice and allocate their correlated idler channels to the other users Bob-Zoe, respectively, which guarantees Alice and every other user share a different time-bin entangled state. Then, fourteen signal channels and the correlated idler channels are allocated to user Bob and the other users Charile-Zoe, respectively, and so on. In this way, 120 time-bin entangled photon pairs are ultimately distributed to the sixteen end users, which ensures that all the users can share a different time-bin entangled photon pair with every other user and a fully connected network topology is successfully constructed. The specific ITU wavelength channels of all users are shown in the wavelength allocation part in Figure 2a. Every user is equipped with a 1-GHZ unbalanced MZI and 2 superconducting nanowire single-photon detectors (SNSPDs, Photec Corp.) with a detect efficiency of over 80%, which is able to implement a passive basis choice. The detection events of the SNSPDs are

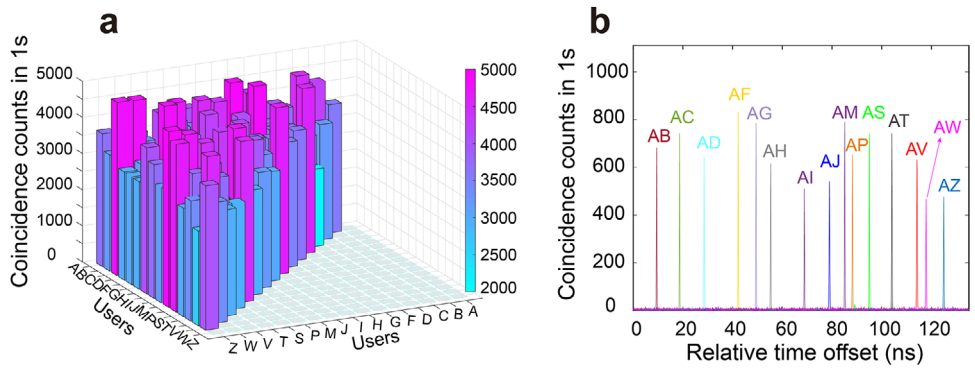

Figure 3. Experimental results between Alice and all other users. a) All the quantum correlations between the sixteen users. b) Temporal cross-correlations between the time traces of Alice's and other users' detectors. The cross-correlation peaks at different positions represent the combinations of two-photon coincidence clicks between Alice and all other users, as indicated by the color labels.

recorded by a time-correlated single photon counting. To ensure that all the users can communicate with other users at the same time, it is of great importance to simultaneously stabilize the relative phase of the end users' interferometers for all wavelength channels, which is quite challenging due to the frequency-sensitive feature of MZI. We design a special unbalanced MZI cascaded phase compensator based on a Fourier-transform setup to overcome this challenge (see Materials and Methods). The photons are randomly detected in the time basis $\{|t\rangle_0, |t\rangle_1\}$ and energy basis $\{(|t\rangle_0 + |t\rangle_1)/\sqrt{2}, (|t\rangle_0 - |t\rangle_1)/\sqrt{2}\}$ and the end users can extract a secure key from their local measurement results for each entangled photon pair following the Bennett-Brassard-Mermin 92 protocol (BBM92).[34]

3. Analysis of the Network Performance

To characterize the performance of the constructed network, we first measure the coincidence count between sixteen users after the entanglement distribution. During the analysis of the network performance, the fiber distances used between the source and the users range from 10 to 40 m, while the total system losses between each pair of end users range from 9 to 11 dB. The experimental measurements are performed simultaneously for every 8 end users due to the limited number of detection devices. To ensure the system has a high signal-to-noise ratio, the down-converted mean photon number μ is controlled to be 0.001 per pulse for each ITU channel. The experimental results are shown in **Figure 3**a, in which any 2 users have coincidence events with a count rate over 10^3 per second with the coincidence count to accidental coincidence count ratios (CAR) of higher than 30. It means that any 2 users share one pair of entangled photons with each other, indicating a fully connected topological graph has been established. It is worth noting that a count rate of over 10^4 per second can be easily achieved by increasing the pump power of the SPDC. As the discrete mode of time-energy entanglement, time-bin entanglement encodes the quantum information in the arrival time of photons directly, which is quite different from polarization entanglement. The end users can detect an arrival-time-difference histogram with 3 peaks for every photon pair due to all the possible path combinations, in which the central peak corresponds to the energy basis $\{(|t\rangle_0 + |t\rangle_1)/\sqrt{2}, (|t\rangle_0 - |t\rangle_1)/\sqrt{2}\}$ and the other 2 correspond to the time basis $\{|t\rangle_0, |t\rangle_1\}$. Therefore, in order to avoid leaking secure information, it is necessary to combine all the time labels of the different detectors for each user into one dataset, where the peak and detector information cannot be distinguished. All users then share the previously merged dataset through an authenticated channel and compute temporal cross-correlation histograms to find the coincidence events. Figure 3b shows the typical temporal cross-correlation functions between Alice and the other users. By using this temporal cross-correlation function, one can easily identify the different entangled photon pairs.

It is of great importance to confirm that the quantum processor distributes high-quality entanglement in all available channels allocated to each user. The quality of the time-bin entanglement of each user is characterized by performing the Franson-type interferometry experiment.[35] We measure the Franson-type interference on a superposition basis by sweeping the phase in the idler interferometer while keeping the phase of the signal interferometer of Alice at 2 non-orthogonal phase settings. **Figure 4**a shows the typical two-photon interference fringes between Alice and Bob. The average visibility is calculated to be $V = (N_{max} - N_{min})/(N_{max} + N_{min}) = 96.7\% \pm 0.9\%$, which exceeds the $1/\sqrt{2}$ visibility necessary for the violation of CHSH Bell inequality.[36,37] Moreover, we further measure the two-photon interference fringes between Alice and other users and calculate the state fidelities using the formula $F = (3V + 1)/4$.[38] Figure 4b shows the typical fidelities for time-bin entanglement between user Alice and all other users. The average fidelities of different entangled states are calculated to be over 95%, which reveals the high quality of time-bin entanglement in the network architecture.

4. QKD based on BBM92 Protocol

The security communication distance and the safe key rate are important indexes in the practical quantum communication network. Next, we demonstrate QKD between the sixteen users by using the standard BBM92 protocol in the established time-bin entangled communication network. By using the temporal cross-correlation functions, the users can obtain the raw key

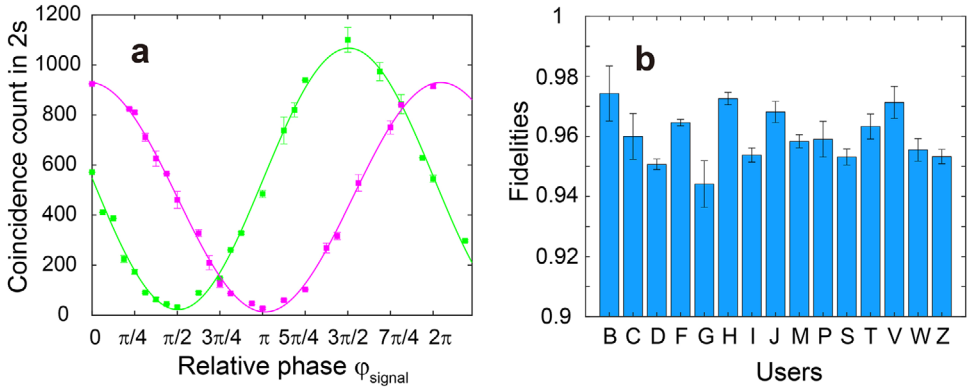

Figure 4. Experimental results for two-photon interference. a) Typical two-photon interference fringes under 2 phase bases between Alice and Bob. b) The fidelities of different entangled states shared by Alice and other users. The uncertainty is calculated by using a Monte-Carlo routine assuming Poisson counting statistics.

after sifting the coincidence events with photons detected on the same basis. According to the security proof of Koashi and Preskill,[39] the secure key rate is given by:

$$R \geq Q\left[1 - fH\left(e_b\right) - H\left(e_p\right)\right] \tag{1}$$

Where f is the error correction efficiency, $H(x) = -x\log_2(x) - (1-x)\log_2(1-x)$ is the binary Shannon entropy, Q is the sifted key rate, e_b and e_p represent bit error rate and phase error rate respectively. According to Gottesman and Lo's security proof, QKD with two-way classical communication can tolerate a higher bit error rate than that with one-way classical communication,[40] which can help to improve the security distance. After performing the two-way classical communication, one can obtain the final key rate as[41]:

$$R \geq Q\left[1 - fH\left(e_b'\right) - H\left(e_p'\right)\right]\left[e_b^2 + \left(1 - e_b\right)^2\right]/2 \tag{2}$$

where $e_b' = e_b^2 /[e_b^2 + (1-e_b)^2]$ and $e_p' \leq 2e_p(1-e_p-e_b)/[e_b^2 + (1-e_b)^2]$. Due to the finite-size effect, there would be a deviation of the phase error rate from the measured bit error rate on the complementary basis.[5,42] The random sampling method can provide an upper bound for this deviation with a fixed failure probability ϵ. The phase error rate is estimated to be $e_p \leq e_b + \sqrt{log(1/\epsilon)(n_t+1)/(2Nn_e)}$, where $N = n_t + n_e$ and n_t, n_e are the raw keys in the time basis and energy basis, respectively, while the quantum bit error rate can be evaluated from the two-photon interference visibility V to be $e_p = (1-V)/2$.[43] After measuring the coincidence counts and accounting for finite key effects with the failure probability of $\epsilon = 10^{-5}$, we calculate the expected secure key rates for Alice and the other users using Equation (2). **Figure** 5a shows the secure key rate versus transmission distance for Alice and the other users in the fully connected network. We first control the down-converted mean photon number to be $\mu = 0.001$ to test the secure key rate of the network system. We measure the quantum cryptographic key for 300 s at a 50 km fiber distance and obtain a typical sifted key rate of 53.9 kbits with an overall quantum bit error rate of 2.9%. The QBERs in a time basis $\{|t\rangle_0, |t\rangle_1\}$ and the energy basis $\{(|t\rangle_0 + |t\rangle_1)/\sqrt{2}, (|t\rangle_0 - |t\rangle_1)/\sqrt{2}\}$ are 2.7% and 3.0%, respectively. To calculate the final secure key rate, we set the error correction efficiency to be $f = 1.16$ and obtain

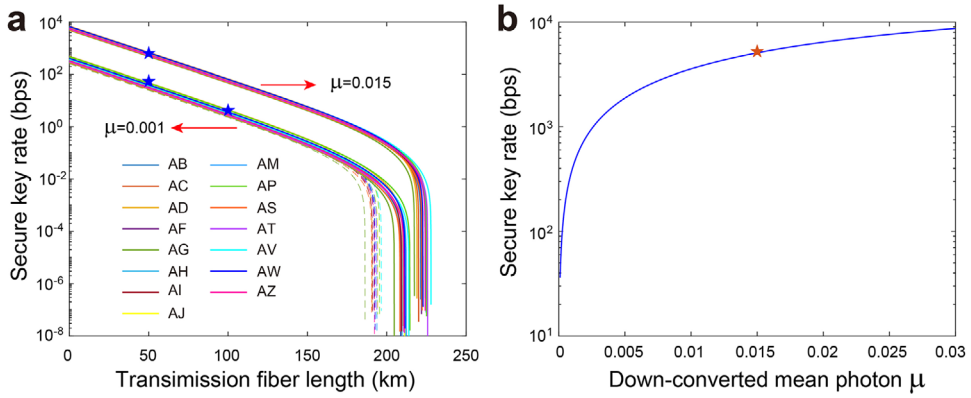

Figure 5. Secure key rate between Alice and the other users in the time-bin entanglement network. a) Secure key rate of the time-bin entangled network as functions of transmission fiber length. The five-pointed blue stars represent the experimental results. The colored solid curves are theoretical predictions of the secure key rate versus transmission distance with two-way communication, while the dashed curves are theoretical predictions without two-way communication. b) Secure key rate of the time-bin entangled network as a function of down-converted mean photon. The five-pointed orange star represents the experimental test.

an average secure key rate of 53 bits/s. Besides, the typical secure key rate at a 100 km fiber distance is obtained to be 4 bits/s with the quantum bit error rate of 3.1%. One can easily improve the key rate by increasing the down-converted mean photon number of the network. Figure 5b shows the available secure key rate of the time-bin entangled network as a function of down-converted mean photon. When the down-converted mean photon is increased to be $\mu = 0.015$, we obtain a secure key rate of 5.1 kbits/s with the quantum bit error rate of 3.4% at 0 km and obtain a secure key rate of 637 bits/s with the quantum bit error rate of 4.3% at a 50 km fiber distance. These experimental and theoretical results show that the end users can achieve QKD with two-way classical communication over a 100-km transmission distance in optical fiber. It is worth noting that using a pump laser with higher repetition frequency, such as 1 Ghz, to pump the SPDC processes can significantly improve the secure key rates of the end users in the network.

5. System Loss and Scalability

Total loss of the quantum system can significantly influence the final safe key rate and security communication distance, which is mainly determined by the quantum processor before the entanglement distribution. For a fully connected entanglement-based quantum network, the system loss primarily results from the coupling loss of the SPDC waveguides and the insertion loss of the multiplexing and demultiplexing modules. In our experiment, the fully connected quantum network architecture is implemented entirely by using commercially available telecommunication equipment, which include 6 40-channel AWGs and sixteen 15-channel thin-film DWDM filters. The AWGs based on integrated planar waveguide technology are leveraged to demultiplex the time-bin entangled photon pairs generated from each PPLN waveguide into 40 ITU channels, while the sixteen thin-film DWDMs are utilized to multiplex the entangled photon pairs to one fiber link to distribute to the end users. The AWGs exhibit insertion losses per channel between 2.5 to 3.2 dB while the insertion losses per channel of the DWDMs vary from 0.5 to 3 dB. **Figure** 6 shows the total loss of all the 120 entangle channels for every 2 users resulting from the coupling loss of the SPDC waveguides and the insertion loss of the multiplexing and demultiplexing modules. The total loss for each correlated channels is ≈10 dB, which means the quantum system can provide high-quality entangled states for the end users.

As 2 significant parameters of a metropolitan quantum network, the secure communication distance and available network users directly determine the network coverage. Compared with continuous-wave pumped entangled networks, our quantum network has more favorable scalability in terms of increasing the secure communication distance and the number of users. In a time-bin entangled network, using a pulse laser with a higher repetition rate as the pump of the entangled source can significantly increase the communication distance and improve the key generation rate. It is worth concerning that how many end users that can be supported in the network while maintaining its performance. In general, it is determined by the signal to noise ratio and quantum resource of the network.

Time-bin entangled network can achieve a better signal to noise ratio than those pumped by a continuous-wave laser. For a continuous-wave pumped fully connected network, the multiplexed photons from all the received wavelength channels may click the SNSPD simultaneously because of the uncertainty of the generation of entangled photon pairs in the time domain. Consequently, the noise level grows higher with the number of users as the count rate of each detector increases but the coincidence rate per link is unchanged. However, this limitation can be overcome to a great extent in a time-bin or polarization entangled network pumped by a pulse laser. In the pulsed-pump scheme, the photon pairs can only generate during the duration of the pump laser. By carefully designing the photon arrival time of the corresponding channels by adjusting the fiber length of different wavelength channels when multiplexing fifteen wavelength channels together in the single mode fibers, the photons of different wavelength channels can be detected at different time positions of the pulse period, which makes the users can communicate with each other in the two-party communication scheme with the help of an additional pulse synchronizing signal. In such way, the quantum processor can significantly reduce the noise count of each node and improves the signal-to-noise ratio of the network, which is beneficial to expand the network architecture and increase the number of users while maintaining the performance.

On the other hand, the available quantum resource, i.e., the number of entangled photon pairs with the wavelength within communication band, also limits the number of users of the network. Although a SPDC source based on single PPLN crystal or waveguide can provide a spectrum with a full width at half maximum of ≈70 nm, the number of the photon pairs in communication band is still limited for a large-scale network with, e.g., 50 users. To construct the fully-connected network topology with 50 end users, the quantum processor needs to multiplex 49 photon channels into one single-mode fiber for each user so that all the users can share a time-bin entangled state with every other user. It means that the quantum processor needs to prepare 1225 quantum entangled photon pairs, a total

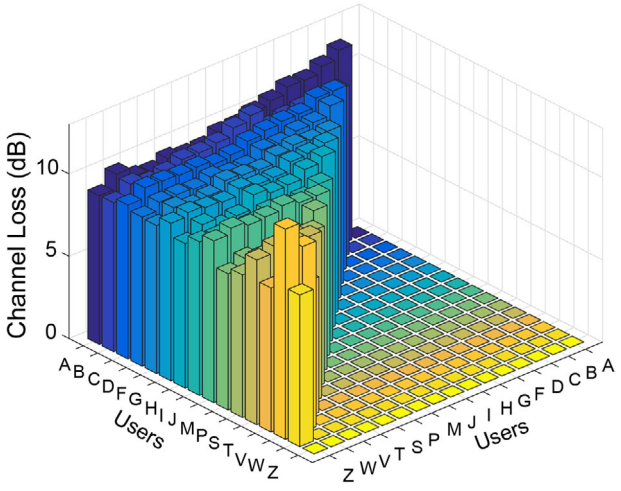

Figure 6. Total losses in each quantum correlated channel between the 16 users.

2450 photon channels, which is quite challenging to implement so many quantum resources by using a traditional source based on a crystal. The time-bin entangled sources implemented in the on-chip multi-channel PPLN waveguides can easily obtain more entangled photon pairs while maintaining the simple structure and compact size of the system. One can generate the required entangled photon pairs through the SPDC processes by pumping more PPLN waveguides. With the increase of users in the network, it is inevitable that 2 channels at same wavelength are multiplexed into one user if only C-band wavelength channels are utilized to construct the network topology. An efficient method to alleviate this problem is to use more wavelength channels, such as the communication S- and L-band, to construct the fully connected network topology. Besides, using both DWDM filters and passive beam splitters flexibly in the wavelength allocation processes can reduce the demand of quantum resource as well as the complexity of multiplexing and demultiplexing module.

Compared with the previously reported polarization entangled network, our time-bin entangled network has 2 distinct advantages in terms of preparing quantum resource and entanglement distribution. The time-bin entangled sources developed in our work can easily implement large-scale quantum resources in a compact integrated platform, while it is difficult for a polarization entangled source based on a Sagnac interferometer to keep a compact size of the quantum system. Besides, time-bin entanglement is based on a coherent superposition of 2 temporal modes and shows intrinsic robustness for propagation through long-distance fiber, while polarization entanglement requires real-time active compensation for polarization drifts in the fiber. In a time-bin entangled network, there may be potential loophole in testing Bell inequality with Franson setup.[44] Fortunately, the post-selection loophole has been addressed in proof-of-principle experiments.[45] An effective method is replacing one passive beam splitter by a balanced MZI acting as an optical switch to address the potential loophole.[46]

6. Conclusion

In conclusion, we implement a sixteen-user time-bin entangled QKD network with a fully connected architecture by using commercially available DWDM technology and a novel time-bin entangled source based on integrated PPLN waveguides. To effectively implement the fully connected network topology, 120 time-bin entangled photon pairs generated by the high-efficiency on-chip PPLN waveguides are multiplexed into 16 single mode fibers for entanglement distribution to the sixteen remote users. The network can provide high-quality time-bin entangled states with the fidelity of higher than 95% and is able to support the sixteen users preforming QKD with each other over a 100-km transmission distance in optical fiber. Our scheme paves an efficient way for implementing large-scale quantum resources in a compact integrated platform, which promises a new potential for constructing a scalable quantum communication network. Such a time-bin entangled fully connected network provides a new option to construct a QKD interconnected networks with dense users in metropolitan areas while minimizes the infrastructure as well as the user hardware needed.

7. Experimental Section

To quantify high-quality entanglement of different end users, one needs to guarantee that the MZIs were indistinguishable in the path travel time differences within the single photon coherence time. To ensure that all the users could communicate with other users at the same time, it was of great importance to simultaneously stabilize the relative phase of the end users' interferometers for all wavelength channels. Figure 2c shows the structure of the MZIs for the end users. The 1-GHZ MZI structure was formed by 2 polarization beam splitters, 2 mirrors, and a PZT mounted on a mirror, while the phase compensator was based on a Fourier-transform setup which consists of 2 diffraction gratings, 2 achromatic lenses, and a spatial light modulator (SLM). In the MZI, the photons polarized vertically pass through the long path, while the other take the short path. After the MZI, the photons were spectrally dispersed by a grating with a diffraction efficiency of 95% and then focused to an elongated spot with the wavelength varying from λ_{min} to λ_{max} by an achromatic lens. A SLM with a resolution of 1920×1200 pixels was placed in the focal plane of the lens to implement the phase control of MZI for different wavelength channels. The SLM could only modulate the phase of horizontally polarized photons and acts as a mirror for vertically polarized photons. Another PBS and a half wave plate rotated at 22.5° were used to eliminate the polarization information and split the photons into 2 parts. Then, one could change the relative phase of the MZIs for different wavelength channels by adjusting the corresponding phase of the diagram loaded on the SLM according to the spatial position of the spot for different wavelength channels. An auxiliary laser was used to feedback-control the PZT to stabilize the phase of the MZIs. Before performing the QKD experiment, the classical interference for the MZIs measured by using continuous wave lasers at the central wavelengths of the involved ITU wavelength channels was first tested. By adjusting the corresponding phase of the diagram loaded on the SLM, the classical interference visibilities for different wavelength channels were measured to be higher than 98%, proving that the Fourier-transform phase compensation setup could simultaneously control the relative phase of the MZIs for different wavelength channels.

Acknowledgements

This work was supported in part by the National Natural Science Foundation of China (Grant Nos. 12192252, 11734011, 11804135, and 12074155), The Foundation for Shanghai Municipal Science and Technology Major Project (Grant No. 2019SHZDZX01-ZX06), SJTU (Grant No. 21×010200828) and Jiangxi Provincial Natural Science Foundation (Grants Nos. 20212ACB201004, 20202ACBL211003).

Conflict of Interest

The authors declare no competing interests.

Author Contributions

Y.H. and Z.Q. contributed equally to this work. X.C. led the project since its conception and supervised all experiments. Y.H., Z.Q and Y.Y. Y.Z. performed the experiment and data analysis. All authors participated in discussions of the results. Y.H. prepared the manuscript with assistance from all other co-authors. Y.L., Y.Z. and X.C. provided revisions.

Data Availability Statement

The data that support the findings of this study are available from the corresponding author upon reasonable request.

Keywords

fully connected network, quantum key distribution, time-bin entanglement

Received: October 10, 2023
Revised: July 28, 2024
Published online:

[1] P. W. Shor, J. Preskill, *Phys. Rev. Lett.* **2000**, *85*, 441.
[2] N. Gisin, G. Ribordy, W. Tittel, H. Zbinden, *Rev. Mod. Phys.* **2002**, *74*, 145.
[3] N. Gisin, R. Thew, *Nat. Photonics* **2007**, *1*, 165.
[4] J. P. Chen, C. Zhang, Y. Liu, C. Jiang, W. J. Zhang, Z. Y. Han, S. Z. Ma, X. L. Hu, Y. H. Li, H. Liu, F. Zhou, *Nat. Photonics* **2021**, *15*, 570.
[5] F. Xu, X. Ma, Q. Zhang, H. K. Lo, J. W. Pan, *Rev. Mod. Phys.* **2020**, *92*, 025002.
[6] S. Wang, Z. Q. Yin, D. Y. He, W. Chen, R. Q. Wang, P. Ye, Y. Zhou, G. J. Fan-Yuan, F. X. Wang, W. Chen, Y. G. Zhu, P. V. Morozov, A. V. Divochiy, Z. Zhou, G.-C. Guo, Z.-F. Han, *Nat. Photonics* **2022**, *16*, 154.
[7] W. Li, L. Zhang, H. Tan, Y. Lu, S. K. Liao, J. Huang, H. Li, Z. Wang, H. K. Mao, B. Yan, Q. Li, Y. Liu, Q. Zhang, C. Z. Peng, L. You, F. Xu, J. W. Pan, *Nat. Photonics* **2023**, *17*, 416.
[8] F. Grünenfelder, A. Boaron, G. V. Resta, M. Perrenoud, D. Rusca, C. Barreiro, R. Houlmann, R. Sax, L. Stasi, S. El-Khoury, E. Hänggi, N. Bosshard, F. Bussières, H. Zbinden, *Nat. Photonics* **2023**, *17*, 422.
[9] S. Wang, W. Chen, Z.-Q. Yin, H.-W. Li, D.-Y. He, Y.-H. Li, Z. Zhou, X.-T. Song, F.-Y. Li, D. Wang, H. Chen, Y.-G. Han, J.-Z. Huang, J.-F. Guo, P.-L. Hao, M. Li, C.-M. Zhang, D. Liu, W.-Y. Liang, C.-H. Miao, P. Wu, G.-C. Guo, Z.-F. Han, *Opt. Express* **2014**, *22*, 21739.
[10] Y. A. Chen, Q. Zhang, T. Y. Chen, W. Q. Cai, S. K. Liao, J. Zhang, K. Chen, J. Yin, J. G. Ren, Z. Chen, S. L. Han, Q. Yu, K. Liang, F. Zhou, X. Yuan, M. S. Zhao, T. Y. Wang, X. Jiang, L. Zhang, W. Y. Liu, Y. Li, Q. Shen, Y. Cao, C. Y. Lu, R. Shu, J. Y. Wang, L. Li, N. L. Liu, F. Xu, X. B. Wang, et al., *Nature* **2021**, *589*, 214.
[11] M. Peev, C. Pacher, R. Alléaume, C. Barreiro, J. Bouda, W. Boxleitner, T. Debuisschert, E. Diamanti, M. Dianati, J. F. Dynes, S. Fasel, *New J. Phys.* **2009**, *11*, 075001.
[12] M. Sasaki, M. Fujiwara, H. Ishizuka, W. Klaus, K. Wakui, M. Takeoka, S. Miki, T. Yamashita, Z. Wang, A. Tanaka, K. Yoshino, *Opt. Express* **2011**, *19*, 10387.
[13] N. B. Lingaraju, H. H. Lu, S. Seshadri, D. E. Leaird, A. M. Weiner, J. M. Lukens, *Optica* **2021**, *8*, 329.
[14] B. Fröhlich, J. F. Dynes, M. Lucamarini, A. W. Sharpe, Z. Yuan, A. J. Shields, *Nature* **2013**, *501*, 69.
[15] S. Wengerowsky, S. K. Joshi, F. Steinlechner, H. Hübel, R. Ursin, *Nature* **2018**, *564*, 225.
[16] Z. D. Li, R. Zhang, X. F. Yin, L. Z. Liu, Y. Hu, Y. Q. Fang, Y. Y. Fei, X. Jiang, J. Zhang, L. Li, N. L. Liu, *Nat. Photonics* **2019**, *13*, 644.
[17] D. Bouwmeester, J. W. Pan, K. Mattle, M. Eibl, H. Weinfurter, A. Zeilinger, *Nature* **1997**, *390*, 575.
[18] H. Takesue, S. D. Dyer, M. J. Stevens, V. Verma, R. P. Mirin, S. W. Nam, *Optica* **2015**, 832.
[19] S. Shen, C. Yuan, Z. Zhang, H. Yu, R. Zhang, C. Yang, H. Li, Z. Wang, Y. Wang, G. Deng, H. Song, L. You, Y. Fan, G. Guo, Q. Zhou, *Light Sci. Appl.* **2023**, *12*, 115.
[20] A. Treiber, A. Poppe, M. Hentschel, D. Ferrini, T. Lorünser, E. Querasser, T. Matyus, H. Hübel, A. Zeilinger, *New J. Phys.* **2009**, *11*, 045013.
[21] Q. C. Sun, Y. F. Jiang, Y. L. Mao, L. X. You, W. Zhang, W. J. Zhang, X. Jiang, T. Y. Chen, H. Li, Y. D. Huang, X. F. Chen, Z. Wang, J. Fan, Q. Zhang, J. W. Pan, *Optica* **2017**, *4*, 1214.
[22] M. Pompili, S. L. Hermans, S. Baier, H. K. Beukers, P. C. Humphreys, R. N. Schouten, R. F. Vermeulen, M. J. Tiggelman, L. dos Santos Martins, B. Dirkse, S. Wehner, *Science* **2021**, *372*, 259.
[23] S. L. N. Hermans, M. Pompili, H. K. C. Beukers, S. Baier, J. Borregaard, R. Hanson, *Nature* **2022**, *605*, 663.
[24] S. Wehner, D. Elkouss, R. Hanson, *Science* **2018**, *362*, eaam9288.
[25] C. L. Degen, F. Reinhard, P. Cappellaro, *Rev. Mod. Phys.* **2017**, *89*, 035002.
[26] L. Yu, C. M. Natarajan, T. Horikiri, C. Langrock, J. S. Pelc, M. G. Tanner, E. Abe, S. Maier, C. Schneider, S. Höfling, M. Kamp, *Nat. Commun.* **2015**, *6*, 8955.
[27] C. Simon, *Nat. Photonics* **2017**, *11*, 678.
[28] S. K. Joshi, D. Aktas, S. Wengerowsky, M. Lončarić, S. P. Neumann, B. Liu, T. Scheidl, G. C. Lorenzo, Ž. Samec, L. Kling, A. Qiu, *Sci. Adv.* **2020**, *6*, eaba0959.
[29] Z. Huang, S. K. Joshi, D. Aktas, C. Lupo, A. O. Quintavalle, N. Venkatachalam, S. Wengerowsky, M. Lončarić, S. P. Neumann, B. Liu, Ž. Samec, *NPJ Quantum Inf.* **2022**, *8*, 25.
[30] X. Liu, X. Yao, R. Xue, H. Wang, H. Li, Z. Wang, L. You, X. Feng, F. Liu, K. Cui, Y. Huang, W. Zhang, *APL Photonics* **2020**, *5*, 076104.
[31] M. Y. Zheng, Q. Yao, B. Wang, X. P. Xie, Q. Zhang, J. W. Pan, *Phys. Rev. Appl.* **2020**, *14*, 034035.
[32] Y. Zhang, H. Li, T. Ding, Y. Huang, L. Liang, X. Sun, Y. Tang, J. Wang, S. Liu, Y. Zheng, X. Chen, *Optica* **2023**, *10*, 688.
[33] O. Gayer, Z. Sacks, E. Galun, A. Arie, *Appl. Phys. B* **2008**, *91*, 343.
[34] C. H. Bennett, G. Brassard, N. D. Mermin, *Phys. Rev. Lett.* **1992**, *68*, 557.
[35] J. D. Franson, *Phys. Rev. Lett.* **1989**, *62*, 2205.
[36] J. F. Clauser, M. A. Horne, A. Shimony, R. A. Holt, *Phys. Rev. Lett.* **1969**, *23*, 880.
[37] I. Marcikic, H. De Riedmatten, W. Tittel, H. Zbinden, M. Legré, N. Gisin, *Phys. Rev. Lett.* **2004**, *93*, 180502.
[38] H. de Riedmatten, I. Marcikic, J. A. W. Van Houwelingen, W. Tittel, H. Zbinden, N. Gisin, *Phys. Rev. A* **2005**, *71*, 050302.
[39] M. Koashi, J. Preskill, *Phys. Rev. Lett.* **2003**, *90*, 057902.
[40] D. Gottesman, H. K. Lo, *IEEE Trans. Inf. Theory* **2003**, *49*, 457.
[41] Q. C. Sun, Y. L. Mao, Y. F. Jiang, Q. Zhao, S. J. Chen, W. Zhang, W. J. Zhang, X. Jiang, T. Y. Chen, L. X. You, L. Li, Y. D. Huang, X. F. Chen, Z. Wang, X. Ma, Q. Zhang, J. W. Pan, *Phys. Rev. A* **2017**, *95*, 032306.
[42] C. H. F. Fung, X. Ma, H. F. Chau, *Phys. Rev. A* **2010**, *81*, 012318.
[43] J. H. Kim, J. W. Chae, Y. C. Jeong, Y. H. Kim, *APL Photonics* **2022**, *7*, 016106.
[44] J. Jogenfors, A. M. Elhassan, J. Ahrens, M. Bourennane, *J. Å. Larsson, Sci. Adv.* **2015**, *1*, e1500793.
[45] F. B. Santagiustina, C. Agnesi, A. Alarcón, A. Cabello, G. B. Xavier, P. Villoresi, G. Vallone, *Optica* **2024**, *11*, 498.
[46] F. Vedovato, C. Agnesi, M. Tomasin, M. Avesani, J. Å. Larsson, G. Vallone, P. Villoresi, *Phys. Rev. Lett.* **2018**, *121*, 190401.